Fractional Order Surge Control of Active Magnetic Bearings Suspended Compressor

Parinya Anantachaisilp [a] and Zongli Lin [b]

[a] Department of Electrical Engineering, Royal Thai Air Force Academy,
171/1 Phaholyotin Rd., Klongthanon Saimai, Bangkok 10220, Thailand, parinya_a@rtaf.mi.th
[b] Charles L. Brown Department of Electrical and Computer Engineering, University of Virginia,
351 McCormick Road, Charlottesville, VA 22904-4743, USA, zl5y@virginia.edu

***Abstract*—This paper demonstrates the design, analysis, and implementation of fractional order PID control (FOPID) for the control of compressor surge in a centrifugal compressor test rig by active magnetic bearings (AMBs). This is the first time that the FOPID controller is designed for and implemented on an AMB system for the surge control objective. In order to achieve the desired design specifications, the controller parameters are tuned by using evolutionary algorithms. Furthermore, a comparison of the performance and efficiency of the FOPID, PID, and an optimal controller is given based on simulation and experimental results.**

I. INTRODUCTION

Proportional-Integral-Derivative (PID) is the most widely used type of controllers in industrial applications (more than 90 percent [1]). This high adoption rate of PID controller for industrial application is likely due to their components having an intuitive physical meaning, i.e., damping and stiffness, which makes them easy to tune. However, the desired performance of a system is sometimes not satisfied by using PID controllers, especially in a complex system such as AMBs. Thus, advanced controllers, which are typically of higher orders, are used instead. However, the design process for advanced controllers is quite complicated and it requires substantial experience to achieve good performance.

Recently, fractional order calculus theory, which is the generalized version of integer order calculus, has been adopted for many applications due to its accuracy for modeling the dynamics of systems and its simplicity in model structure to represent high order processes [2-7]. Fractional order control is one of the fields that many researchers and engineers are interested in because the response of a system with a fractional order controller is not restricted to a sum of exponential functions, and, as a result, a wide range of responses neglected by integer order calculus could be approached. One of the most popular fractional order controllers is the generalized PID controller, which is also called a fractional order PID (FOPID) controller. FOPID has two extra parameters, the non-integer order of integral and derivative terms, in comparison with the integer order PID controller. FOPID control can improve performance and robustness compared to conventional PID control in many applications while keeping the control structure simple. This suggests that an FOPID controller has good potential to reduce the gap between the simplicity of the controller structure and high closed-loop performance aspects as mentioned above.

Moreover, fractional order control concept has been studied and implemented for the rotor suspension by using radial AMBs as described in [8]. In this paper, it will demonstrate the design, analysis, and implementation of an FOPID controller for suppressing vibration and surge in a centrifugal compressor by using thrust magnetic bearing. Furthermore, a comparison of the performance and efficiency of the FOPID, integer order PID (IOPID), and advanced controller based on simulation and experimental results, conducted on the centrifugal compressor test rig equipped with AMBs at the Rotating Machinery and Control Laboratory (ROMAC), the University of Virginia is discussed.

II. SYSTEM DESCRIPTION

For the purpose of investigating the capability of AMBs in high-speed compressor applications, the single-stage centrifugal compressor equipped with AMBs was built and commissioned in the Rotating Machinery and Control Laboratory (ROMAC) at the University of Virginia, as shown in Figures 1 and 2. Specifically, this test rig is used as a platform to demonstrate flow instabilities caused by surge in a centrifugal compressor. The rotor is levitated by two radial AMBs for smooth rotation without mechanical contact. The rotor is supported axially by the thrust AMB, which is also used to modulate the impeller tip clearance for the purpose of surge control. The designed maximum operational speed is 23,000 rpm, which requires a power supply of 52 kW. Within the operating speed range (maximum at 23,000 rpm), the rotor is considered to be a rigid rotor since the first bending mode is at 40,792 rpm. The rotor has a length of 0.517 m and is 27 kg in mass. AMBs used for radial suspension are 12 pole E-core design. The 12 poles are separated into four quadrants. The widths of the primary and secondary poles are 27.94 mm and 13.97 mm, respectively. Each pole has 51 turns of 17 AWG wire. The stators of the radial AMBs are laminated in order to reduce the eddy current effect. The

designed maximum load capacity per quadrant is 1414 N and the nominal air gap is 0.5 mm.

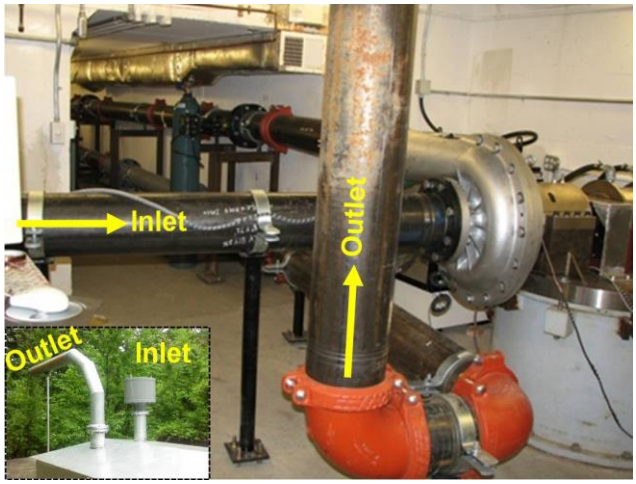

Figure 1. Centrifugal compressor test rig.

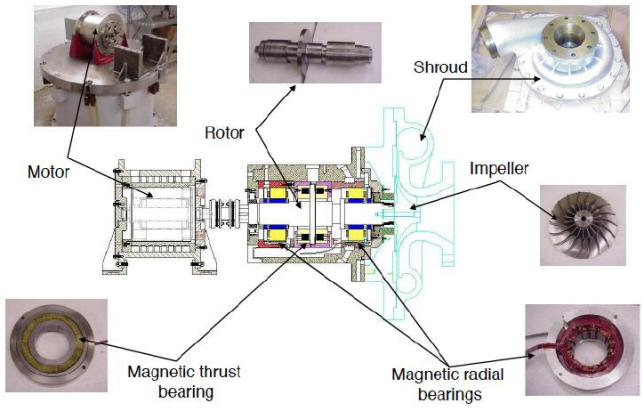

Figure 2. Components of the centrifugal compressor.

The corresponding values of negative stiffness K_x and current gain K_i were obtained experimentally and summarized in Table 1. The instrumentation properties are summarized in Table 2.

Table 1. AMB properties.

Radial AMB	I_b (A)	K_x (N/m)	K_i (N/A)
Motor side	3	1.27×10^6	199.34
Compressor side	4	2.26×10^6	265.86
Thrust AMB	3	4.23×10^6	664.12

Table 2. Instrumentation properties.

AMB	Motor Side	Compressor Side	Thrust
Amplifier gain (A/V)	1.5	1.5	1.5
Amplifier bandwidth (rad/s)	5026.5	5026.5	5026.5
Sensor gain (V/m)	3.937×10^4	3.937×10^4	3.937×10^4
Sensor bandwidth (rad/s)	1.26×10^4	1.26×10^4	1.26×10^4
Maximum slew rate (N/s)	2.2×10^6	2.2×10^6	1.9×10^6

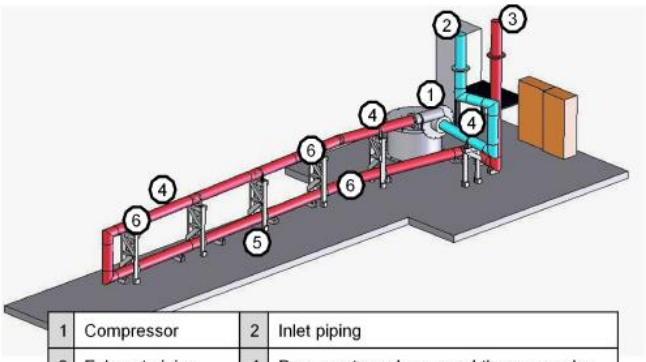

Figure 3. Test rig layout.

The compression system consists of three main components, the centrifugal compressor, the modular ducting system, and the throttle valve. The location of each component installed in the system is illustrated in Figure 3. The compressor is a single stage with an unshrouded impeller as shown in Figure 2. It was manufactured and donated by Kobe Steel, Ltd, Japan. The compressor design parameters are summarized in Table 3. For this compressor, the impeller tip clearance, which is the axial clearance between the static shroud and the impeller tip, is regulated by the thrust AMB.

Table 3. Compressor parameters.

Parameter	Unit	Value
Maximum speed	rpm	23,000
Design mass flow rate	kg/s	0.833
Design pressure ratio	-	1.68
Impeller tip diameter	mm	250
Impeller tip blade height	mm	8.21
Inducer hub diameter	mm	56.3
Inducer diameter	mm	116.72

Modular ducting system allows the change of the plenum volume, which in turn allows flexibility in controlling the compression system behavior. The ducting system design parameters are summarized in Table 4.

Table 4. Ducting system parameters.

Parameter	Unit	Value
Piping diameter	m	0.203
Inlet piping length	m	5.2
Exhaust piping length	m	21.3
Plenum volume #1	m^3	0.07
Plenum volume #2	m^3	0.23
Plenum volume #3	m^3	0.49

Along the pipeline, the throttle valve is installed (with three possible locations as shown in Figure 3) to control the steady state flow rate. Changes in the flow rate will change the

volume in the plenum. These throttle valves are common commercially available butterfly type valves. Pressure transducers, thermocouples, and orifice flow meters are installed in the compression system in order to measure the pressure, temperature, and mass flow rate respectively. The location of these sensors can be found in Figure 3. These measurements will be used to generate the compressor characteristic curve as well as to provide information for the surge controller. Additionally, the compressor is driven by an induction motor with the output power of 125 kW at the maximum speed of 29,680 rpm. Due to the high power density of the motor, a cooling system is required when operating continuously at high speeds. Therefore, a chiller is installed to circulate the refrigerant fluid in the cooling system of the motor. In addition, rotor suspension and surge control algorithms are implemented by the computer operating on a real-time RTLinux operating system, with a sampling rate of 5kHz. Input signals to the control computer include rotor position measurements from sensors and the plenum pressure rise measurement, which are sampled at the same time interval. The temperature and flow measurements are collected by the Labview data acquisition system, which is used to operate the motor drive and throttle valve as well. For the user's safety, these two computers can be controlled remotely from a control room separated from the compressor test rig. The layout drawing of the control/data-acquisition system is illustrated in Figure 4.

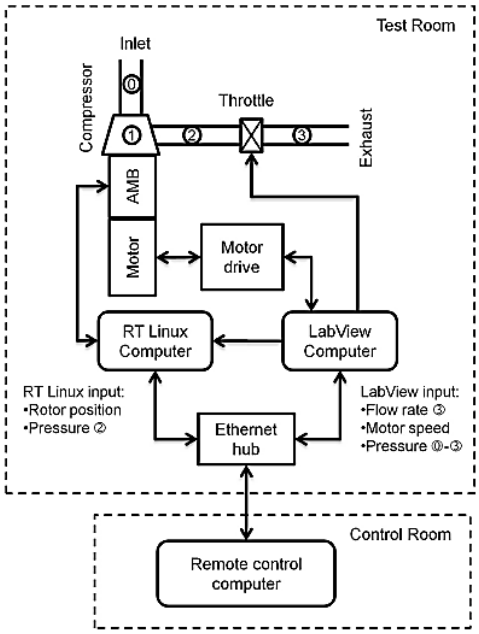

Figure 4. Layout of the control/data-acquisition system of the test rig [9]

III. DESIGN OF FRACTIONAL ORDER SURGE CONTROLLER

The objective in the surge control design is to stabilize the compression system in the surge condition, where the equilibrium operating point is beyond the surge line limit. As shown in Figure 5, the two inputs of the surge controller K from the compression system G are the compressor mass flow rate and the plenum pressure rise. The controller output is the reference impeller tip clearance, which is fed into the closed-loop thrust AMB system, T_{amb}. The thrust AMB controller will track the desired tip clearance specified by the surge controller in order to induce an appropriate amount of pressure rise for surge stabilization. In the actual implementation, it is impossible to have perfect tracking by the thrust AMB due to external disturbances. This means that the performance of the surge controller will be degraded. Because of this limitation, the surge control design must take into account disturbances, which can impact the interaction between the surge and thrust AMB controllers. Moreover, Yoon et al. suggested in [9] that the closed-loop system shown in Figure 5 can be restructured as shown in Figure 6.

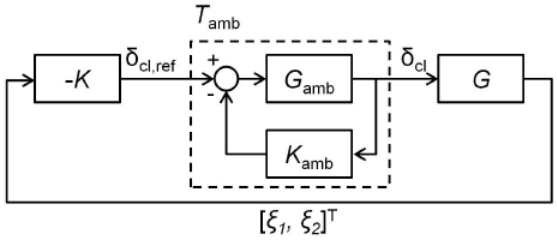

Figure 5. Closed-loop compression system with surge controller diagram

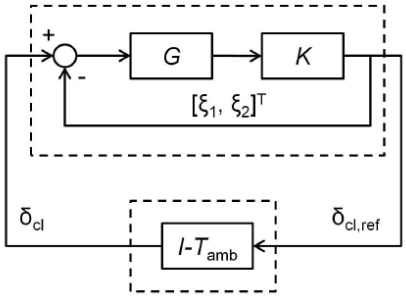

Figure 6. Modified closed-loop compression system with surge controller

This way the closed-loop dynamics of the compression system and the rotor/thrust AMB system are separated.

In this work, the surge controller for each input-output pair consists of a fractional PD controller (the structure of the controller is shown in Equation (1) where μ is the order of the derivative part, while K_P and K_D are the controller gains), a lowpass filter, and a notch filter.

$$C_{FOPD} = K_P + K_D s^{\mu} \tag{1}$$

The center frequency of the notch filter is placed at a frequency slightly lower than the critical frequency of the system (approximately 5-10 Hz lower) so that the designed controller can provide more damping at the critical frequency. The structure of the notch filter is

$$G_{notch} = \frac{s^2 + \omega_n^2}{s^2 + 2\zeta\omega_n s + \omega_n^2}$$

where ω_n is the center frequency of the notch and ζ indicates the notch sharpness. The objectives for the surge controller tuning are adopted from [9] as follows.

1. Stability of closed-loop system: The closed-loop stability condition is derived from the Small Gain Theorem. The optimization goal is to have $J_1 < 1$.

$$J_1 = \left\| (I + KG)^{-1} KG(I - T_{amb}) \right\|_\infty$$

2. Robust stability condition:

$$J_2 = \left\| W_1 S_i K G W_3 \right\|_\infty$$

3. Control effort according to the reference equilibrium operating point condition:

$$J_3 = \left\| W_1 S_i K W_4 \right\|_\infty$$

4. Transmission of the input disturbance to the plant output signal condition:

$$J_4 = \left\| W_2 S_o G W_3 \right\|_\infty$$

5. Closed-loop dynamics from the reference equilibrium operating point to the plant output signal condition:

$$J_5 = \left\| W_2 S_o G K W_4 \right\|_\infty$$

where $S_i = (I + KG)^{-1}$, $S_o = (I + GK)^{-1}$, and the weighting functions are as defined in [9], which are based on the interconnected system shown in Figure 7, as follows.

$$W_1(s) = I,$$
$$W_2(s) = 0.001I,$$
$$W_3(s) = 2\frac{(s+0.1)}{(s+300)}I,$$
$$W_4(s) = 2000\frac{(s+0.1)}{(s+3000)}\begin{bmatrix} 1.5 & 0 \\ 0 & 1 \end{bmatrix}$$

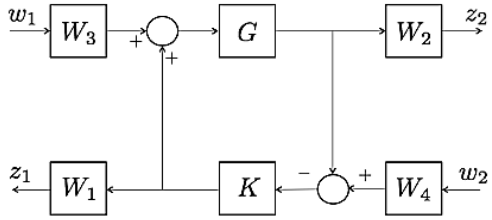

Figure 7. Interconnected system for the design of the surge controller

All objective functions will be combined as a single cost function during the optimization process, which is as follows.

$$J = \max\left\{J_1, J_2, J_3, J_4, J_5\right\}$$

The optimization goal is to have the infinity norm of all objective functions to be smaller than 1. Within this study, all controller parameters are tuned using the Genetic Algorithm (GA) [10-12], the Differential Evolution (DE) algorithm [13,14] and the Particle Swarm Optimization (PSO) algorithm [15,16]. Table 5 summarizes the resulting infinity norms of the objective functions of all tuning methods. In addition, the resulting magnitude plots of all objectives, except the stability objective, resulting from the three different tuning methods are shown in Figure 7. It can be observed that only the DE algorithm results in the maximum magnitude of the objective functions smaller than 1. Therefore, this controller design will be used for implementation and comparison with the other kind of controllers. Table 6 summarizes the values of the FOPD controller and the notch filter parameters obtained from the DE optimization.

Table 5. Comparison of the performance of different tuning methods.

Controller characteristics	GA	DE	PSO
Infinity norm of objective functions	1.048	0.991	1.019

Table 6. Parameters of tuned fractional surge controller.

Input - Output	K_P	K_D	μ	ζ	ω_n

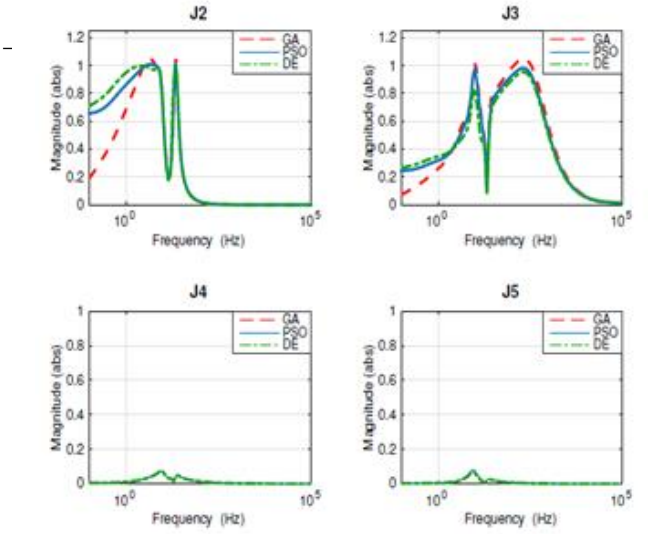

Figure 7. Magnitudes of objective functions from three tuning methods

For comparison, the conventional PID controller is tuned based on the same objectives and algorithms as the FOPID controller. Moreover, the surge H_∞ controller that was designed for the same compression system reported in [9] is also considered. Table 7 summarizes the infinity norms of all objectives of the IOPID, the FOPID, and the H_∞ controllers, and their magnitude plots are illustrated in Figure 8.

Table 7. Performance of surge controllers.

Controller characteristics	PID	FOPID	H_∞
Infinity norm of objectives	1.143	0.991	0.969
Controller order as implemented	6	6	7

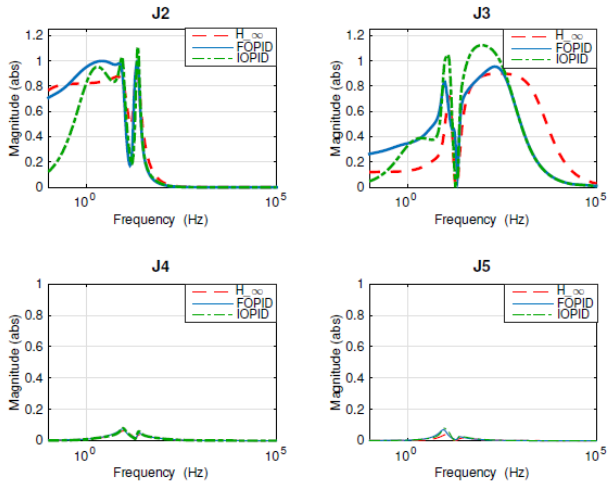

Figure 8. Magnitudes of objective functions for all controllers.

IV. SIMULATION RESULTS OF SURGE CONTROL

With the derived surge controller, the simulation was carried out on the nonlinear compression system model. The closed-loop dynamics of the thrust AMB is represented by a third order low-pass Butterworth filter with the cutoff frequency of 70 Hz. Figure 9 shows the simulation results of the compression system when the surge controller is unactivated. In the simulation, the throttle valve was gradually closed from 20% opening (stable) to 16% opening (unstable), where the crossing between the two regions occurs at 18.5% opening. Since there is no surge controller activated, the variation of the impeller tip clearance remains zero as shown in Figure 9(b). Figure 9(c) shows that the states ξ_1 and ξ_2 of the compression system demonstrate large oscillation magnitudes after the system enters the surge region. Similarly, the value of the plenum pressure rise ψ_p demonstrates large oscillation magnitudes after the system enters the surge region as shown in Figure 9(d).

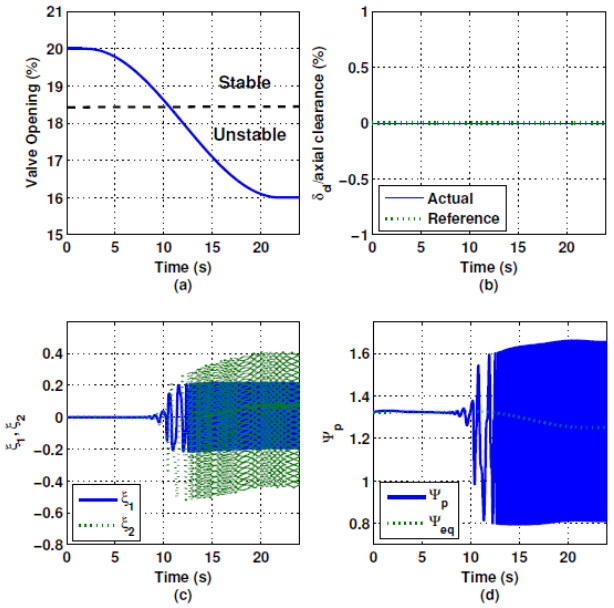

Figure 9. Simulation results of the compression system with the surge controller unactivated.

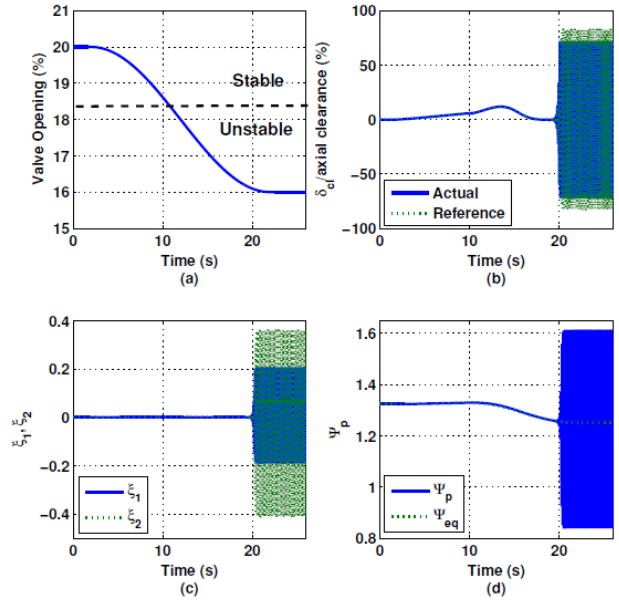

Figure 10. Simulation results of the compression system under the PID surge controller.

Figure 10 shows the simulation results of the compression system when using the PID controller that is tuned with the same algorithm and objectives as for the FOPID controller. This PID controller can stabilize the compression system even after the system enters the surge region, but the system becomes unstable at approximately 16.2% of throttle valve opening. Figure 11 shows the simulation results of the compression system when the H_∞ surge controller is activated. The compression system is stabilized even when it enters the unstable region by modulating the impeller tip clearance as shown in Figure 11(b).

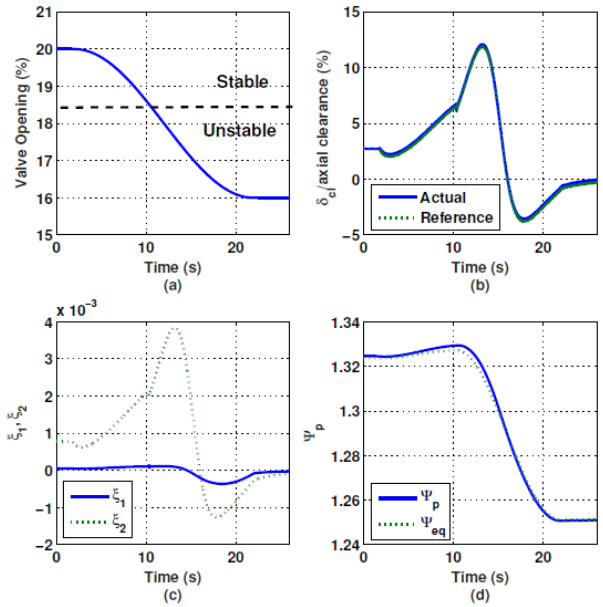

Figure 11. Simulation results of the compression system under the H_∞ surge controller.

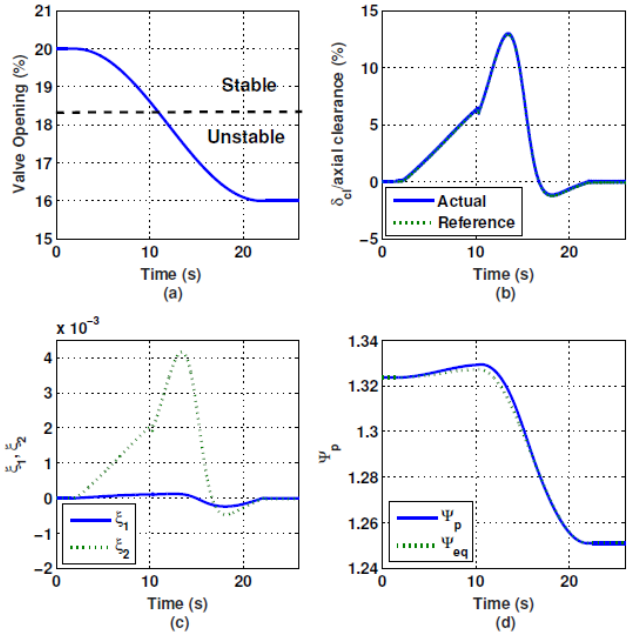

Figure 12. Simulation results of the compression system under the FOPID surge controller.

Both states ξ_1 and ξ_2 of the compression system are still stable even after the system enters the unstable region as shown in Figure 11(c). Finally, Figure 11(d) shows the values of the plenum pressure rise ψ_p and the equilibrium pressure rise ψ_{eq} that stabilize the compression system. Similar to the performance provided by the H_∞ surge controller, the FOPID surge controller stabilizes the compression system. In addition, the peak value of the tip clearance modulation is approximately the same as in the case of the H_∞ surge controller as shown in Figure 12(b). Also, the maximum values of the states shown in Figure 12(c) stay stable after the system enters the surge region. It can be seen that the closed-loop system with the FOPID surge controller is more robust than in the case of the PID surge controller. Finally, the simulation results demonstrate that the FOPID surge controller can stabilize the compression system to the same level as the H_∞ surge controller during the simulation.

V. EXPERIMENTAL RESULTS OF SURGE CONTROL

The surge controller will be activated when needed on top of the rotor suspension controllers that are always active throughout the operating period. Since the surge control implementation will be tested at 16,290 rpm, which will store high potential energy, the accidental contact by improper surge controller implementation can cause more damage to the compressor than the surge instability. Therefore, a safety mechanism for the surge controller activation is required. Within this study, prior to the surge controller activation, rotor vibration is checked. If rotor vibration is within the predefined limit, the surge controller is engaged in the control process. Then, the reference of the rotor axial position computed by the surge controller is limited to $\pm$ 70% of the available axial clearance. Otherwise, the reference of the rotor axial position is set to zero for a safe operating environment. The flow chart of the surge controller operation is illustrated in Figure 13. With the rotor spinning at 16,290 rpm, the system is driven into surge by gradually closing down the throttle valve starting from a 21.0% opening, in 0.1% decrements, for smooth operation. Figure 14 shows that the compression system enters the surge at a 17.8% of the throttle valve opening in the absence of the surge controller. The frequency response plot shows large peaks at approximately 7 Hz and 21 Hz, which agrees with the prediction of the compression system characteristics described in [9].

For the next surge test, the IOPID surge controller is activated under the same testing condition as for the previous test. Figure 15 shows the frequency response of the measured plenum pressure rise when the IOPID surge controller is activated. The large peaks of the frequency response initiate at a 16.9% throttle valve opening position. The result shows that, with the IOPID surge controller activated, the compression system can operate stably beyond the original surge limit. Figure 16 shows the non-dimensional mass flow rate and the plenum pressure rise on the characteristic curve during stable operation. The measurements with the surge controller unactivated are marked by `o'. These values are measured from 21% valve opening until 17.8%, where the surge initiates. The measurements marked by `x' represent the extended operating points when the IOPID controller is activated. It can be observed that the surge limit is extended in terms of the mass flow range from the uncontrolled case by 11.97%.

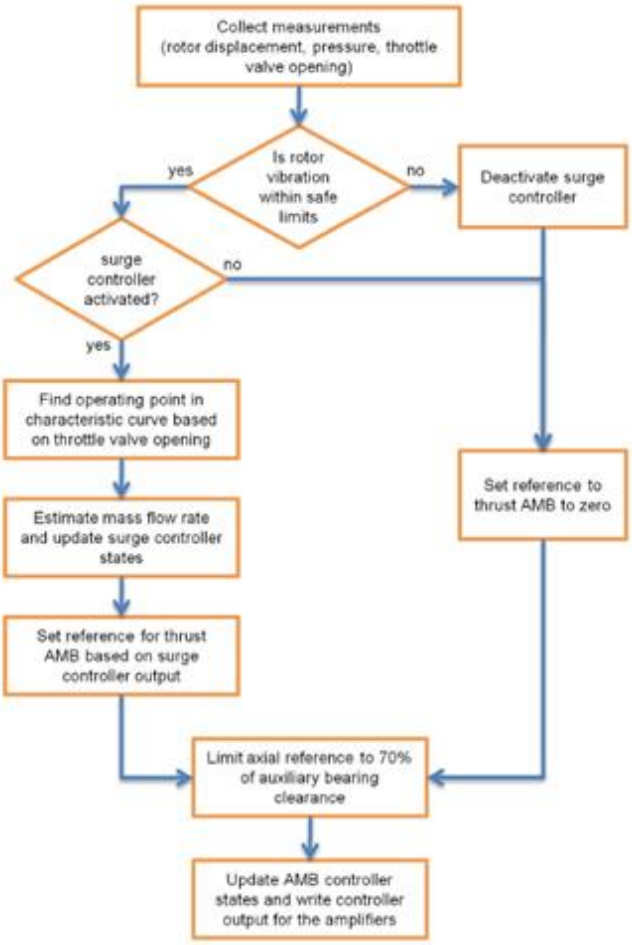

Figure 13. Flow chart of the surge control implementation [9]

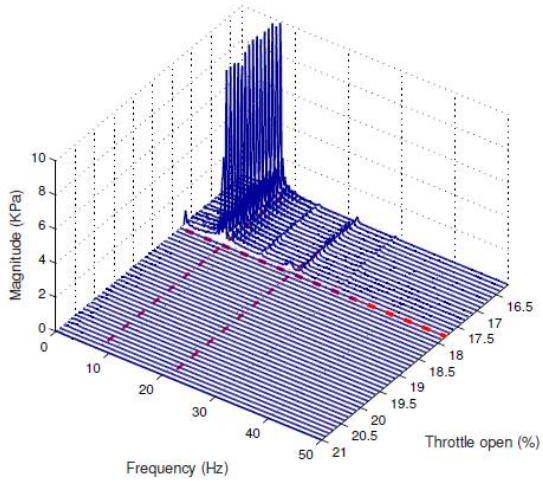

Figure 14. Waterfall plot of the frequency response of the measured Plenum pressure signal at 16,290 rpm with the surge controller unactivated.

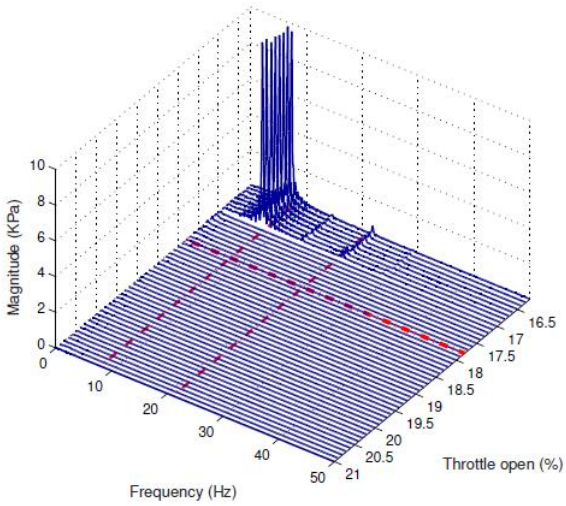

Figure 15. Waterfall plot of the frequency response of the measured Plenum pressure signal at 16,290 rpm with the IOPID surge controller activated.

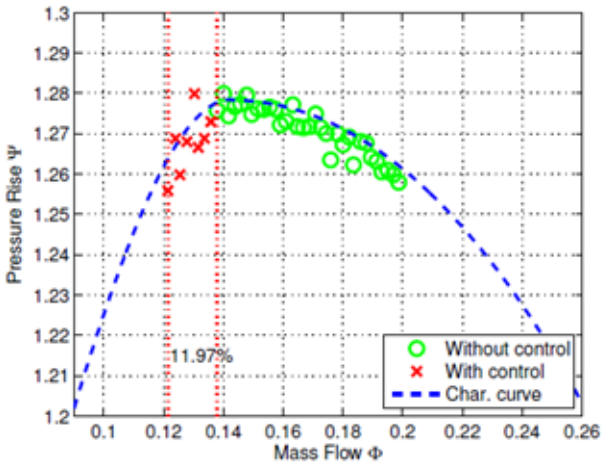

Figure 16. Compressor steady-state operation on the characteristic curve at 16,290 rpm with the IOPID surge controller activated and unactivated, respectively.

In addition, the measured and the reference of the ratio of the impeller tip clearance and the available axial clearance are shown in Figure 17(b). The maximum value of the impeller tip clearance is about 40% of the available axial clearance. This shows that the IOPID surge controller can operate stably with some axial position margin compared with the predefined 70% of the available clearance. Figure 17(c) shows the values of the surge controller states ξ_1 and ξ_2, when the throttle valve is opened at 17.0%. Then, the non-dimensional measured pressure rise and its equilibrium values are illustrated in Figure 17(d).

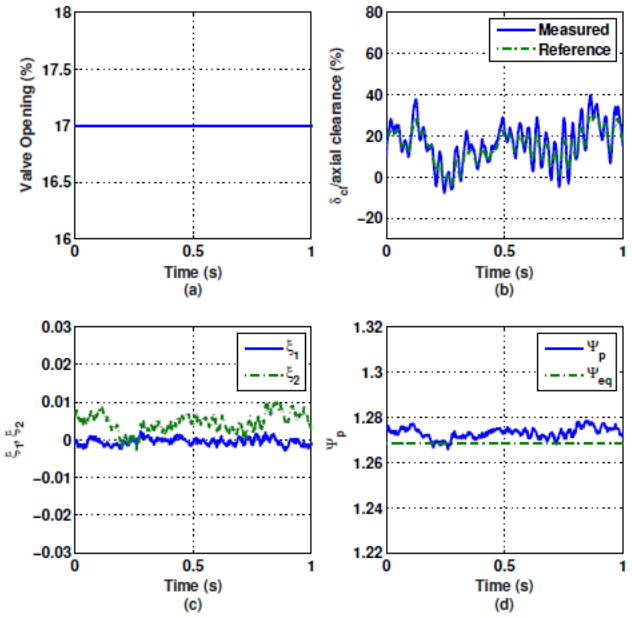

Figure 17. Experimental results of the compression system under the IOPID surge controller at 17.0% throttle valve opening.

For the case of the FOPID surge controller test, Figure 18 shows the frequency response of the measured plenum pressure rise. It can be noticed that the compression system enters surge when the throttle valve opens at 16.2%, which further extends the surge limit where the IOPID surge controller remains stable until 17.0% opening.

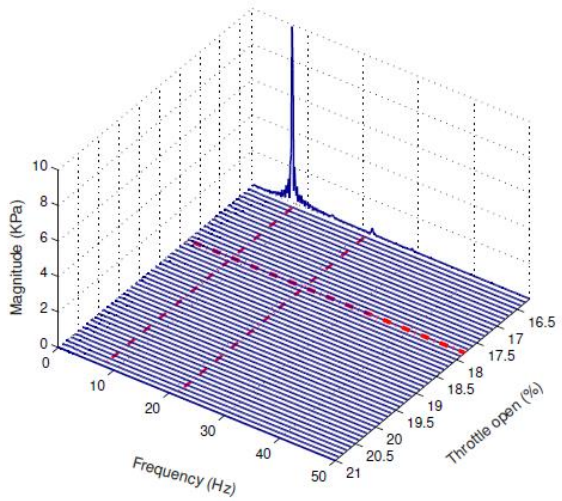

Figure 18. Waterfall plot of the frequency response of the measured Plenum pressure signal at 16,290 rpm with the FOPID surge controller activated.

Figure 19 shows the non-dimensional mass flow rate and the plenum pressure rise on the characteristic curve during stable operation with the FOPID surge controller activated after the surge limit. The measurements with the FOPID surge

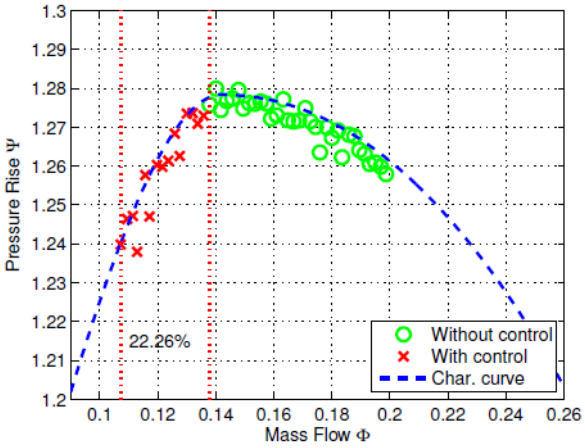

Figure 19. Compressor steady-state operation on the characteristic curve at 16,290 rpm with the FOPID surge controller activated and unactivated, respectively.

controller unactivated are marked by `o'. These values are measured from 21% valve opening until 17.8%, where the surge initiates. The measurements marked by `x' represent the extended operating points when the FOPID controller is activated. It can be observed that the surge limit is extended in terms of the mass flow range from the uncontrolled case by 22.26%. In addition, the maximum value of the impeller tip clearance is approximately 35% of the available axial clearance as shown in Figure 20(b). This shows that the FOPID surge controller results in a slightly larger axial clearance margin than the IOPID surge controller case. Figure 20(c) shows the values of the surge controller states ξ_1 and ξ_2, when the throttle valve is opened at 16.3%. The non-dimensional measured pressure rise and its equilibrium values are illustrated in Figure 20(d).

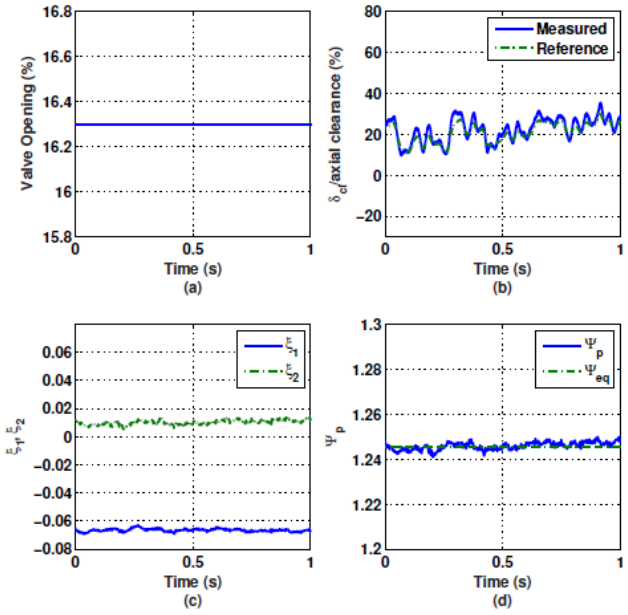

Figure 20. Experimental results of the compression system under the FOPID surge controller at 16.3% throttle valve opening.

Finally, for the case when the H_∞ surge controller is activated, Figure 21 shows that the compression system remains stable when the throttle valve opens as small as 16.2%. This extends the throttle valve opening for another 0.1% beyond the FOPID surge controller case. Figure 22 shows the non-dimensional mass flow rate and the plenum pressure rise on the characteristic curve during stable operation with the H_∞ surge controller activated after the surge limit. The measurements with the surge controller unactivated are marked by `o'. These values are measured from 21% valve opening until 17.8%, where the surge initiates. The measurements marked by `x' represent the extended operating points when the H_∞ controller is activated. It can be observed that the surge limit is extended in terms of the mass flow range from the uncontrolled case by 22.92%.

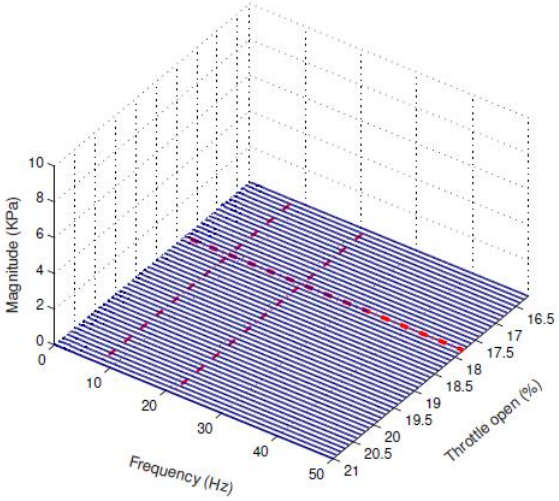

Figure 21. Waterfall plot of the frequency response of the measured Plenum pressure signal at 16,290 rpm with the H_∞ surge controller activated.

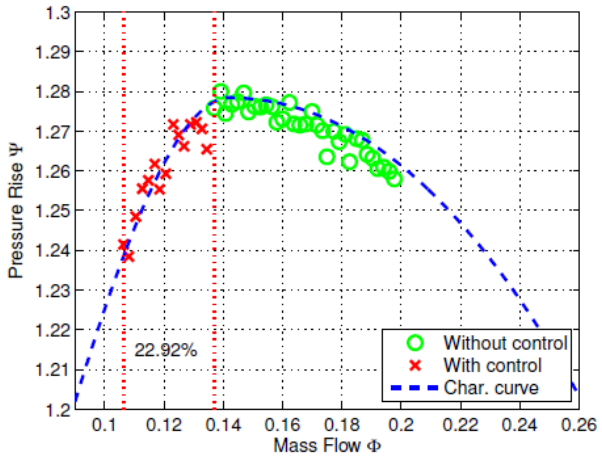

Figure 22. Compressor steady-state operation on the characteristic curve at 16,290 rpm with the H_∞ surge controller activated and unactivated, respectively.

In addition, the maximum value of the impeller tip clearance is about 35% of the available axial clearance as shown in Figure 23(b). This shows that the H_∞ surge controller can operate stably with approximately the same axial clearance margin as the FOPID surge controller case. Figure 23(c) shows the values of the surge controller states ξ_1 and ξ_2, when the throttle valve is opened at 16.2%. The non-dimensional measured pressure rise and its equilibrium values are illustrated in Figure 23(d).

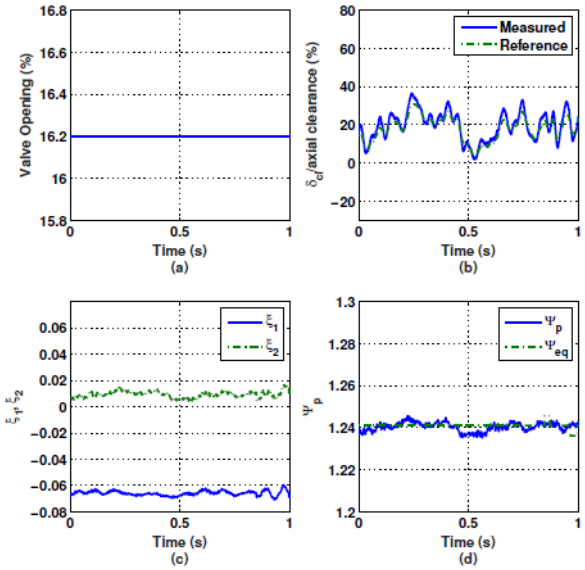

Figure 23. Experimental results of the compression system under the H_∞ surge controller at 16.2% throttle valve opening.

VI. SUMMARY

This paper presents the design of the FOPID surge controller with three different tuning methods namely, the Genetic Algorithm (GA) method, the Differential Evolution (DE) method, and the Particle Swarm Optimization (PSO) method. Simulation results show that the FOPID surge controller tuned by the DE method achieves the best performance. Therefore, this design is used for the implementation on the compressor test rig. For comparison, the IOPID surge controller was designed based on the same objectives and optimization algorithm. Simulation results show that the IOPID controller can stabilize the compression system beyond the surge limit, but not as much as the FOPID and H_∞ surge controllers can. These simulation results are then validated by experimental testing on the compressor test rig. The experimental results show that the IOPID surge controller can extend the surge limit in terms of the mass flow range from the uncontrolled case by 11.96%. For the case of the FOPID and the H_∞ surge controllers, the surge limit is extended by 22.26% and 22.92%, respectively.

REFERENCES

[1] Astrom, K. J., and Hagglund, T., "Advanced PID Control," *ISA, Research*, Triangle Park, NC, 2006.

[2] Bagley, R.L.; Calico, R. Fractional order state equations for the control of viscoelastically damped structures. J. Guid. Control Dyn. 1991, 14, 304–311.

[3] Oustaloup, A.; Mathieu, B.; Lanusse, P. The crone control of resonant plants: Application to a flexible transmission. Eur. J. Control 1995, 1, 113–121.

[4] Aldair, A.A.; Wang, W.J. Design of fractional order controller based on evolutionary algorithm for a full vehicle nonlinear active suspension systems. Int. J. Control Autom. 2010, 3, 33–46.

[5] Calderon, A.J.; Vinagre, B.M.; Feliu, V. Fractional order control strategies for power electronic buck converters. Signal Process. 2006, 86, 2803–2819.

[6] Ferreira, N.F.; Machado, J.T. Fractional-order hybrid control of robotic manipulators. In Proceedings of the 11th International Conference on Advanced Robotics (ICAR 2003), Coimbra, Portugal, 30 June–3 July 2003; pp. 393–398.

[7] Gabano, J.-D.; Poinot, T. Fractional modelling and identification of thermal systems. Signal Process. 2011, 91, 531–541.

[8] Anantachaisilp, P., and Lin, Z., "Fractional Order PID Control of Rotor Suspension by Active Magnetic Bearings." Actuators. Vol. 6. No. 1. Multidisciplinary Digital Publishing Institute, 2017.

[9] Yoon, S. Y., Lin, Z., and Allaire, P., "Control of Surge in Centrifugal Compressors by Active Magnetic Bearings," Springer, 2012.

[10] Chang, L.Y.; Chen, H.C. Tuning of fractional PID controllers using adaptive genetic algorithm for active magnetic bearing system. WSEAS Trans. Syst. 2009, 8, 158–167.

[11] Chang, F.-K.; Lee, C.-H. Design of fractional PID control via hybrid of electromagnetism-like and genetic algorithms. In Proceedings of the Eighth International Conference Intelligent Systems Design and Applications (ISDA08), Kaohsiung, Taiwan, 26–28 November 2008; pp. 525–530.

[12] Cao, J.-Y.; Liang, J.; Cao, B.-G. Optimization of fractional order PID controllers based on genetic algorithms. In Proceedings of the 2005 International Conference Machine Learning and Cybernetics, Guangzhou, China, 18–21 August 2005; pp. 5686–5689.

[13] Biswas, A.; Das, S.; Abraham, A.; Dasgupta, S. Design of fractional-order PID controllers with an improved differential evolution. Eng. Appl. Artif. Intell. 2009, 22, 343–350.

[14] Chang, W.-D. Two-dimensional fractional-order digital differentiator design by using differential evolution algorithm. Digit. Signal Process. 2009, 19, 660–667.

[15] Bingul, Z.; Karahan, O. Tuning of fractional PID controllers using PSO algorithm for robot trajectory control. In Proceedings of the 2011 IEEE International Conference Mechatronics (ICM), Istanbul, Turkey, 13–15 April 2011; pp. 955–960.

[16] Cao, J.-Y.; Cao, B.-G. Design of fractional order controllers based on particle swarm optimization. In Proceedings of the 2006 1ST IEEE Conference Industrial Electronics and Applications, Singapore, 24–26 May 2006; pp. 1–6.